Dissolved [129]Xe lung MRI with 4-echo 3D radial spectroscopic imaging: quantification of regional gas transfer in idiopathic pulmonary fibrosis

Guilhem J. Collier[1*], James A. Eaden[1], Paul J.C. Hughes[1], Stephen M. Bianchi[2], Neil J. Stewart[1], Nick D. Weatherley[1], Graham Norquay[1], Rolf F. Schulte[3], Jim M. Wild[1]

[1]POLARIS, Imaging Sciences, Department of Infection, Immunity & Cardiovascular Disease, University of Sheffield, UK

[2] Academic Directorate of Respiratory Medicine, Sheffield Teaching Hospitals NHS Foundation Trust, Sheffield, UK

[3] GE Healthcare, Munich, Germany.

[*]Corresponding Author: Dr. Guilhem J. Collier

Email: g.j.collier@sheffield.ac.uk

Address: MRI unit, University of Sheffield, C Floor, Royal Hallamshire Hospital,

Glossop Road, Sheffield, S10 2JF, UK

Phone Number: + 44 (0)114 2159145

Word Count: (4665 words, 7 figures, 1 table)

Running title: Dissolved [129]Xe spectroscopic pulmonary imaging in IPF

Keywords: hyperpolarized [129]Xe, Lung, IPF, spectroscopic imaging

Abstract (238/250words)

Purpose: Imaging of the different resonances of dissolved hyperpolarized xenon-129 in the lung is performed using a 4-echo flyback 3D radial spectroscopic imaging technique and is evaluated in healthy volunteers (HV) and subjects with idiopathic pulmonary fibrosis (IPF).

Methods: 10 HV and 25 subjects with IPF underwent dissolved ^{129}Xe MRI at 1.5 T. IPF subjects underwent same day pulmonary function tests to measure forced vital capacity and the diffusion capacity of the lung for carbon monoxide (DL_{CO}). A 4-point echo time technique with k-space chemical-shift modelling of gas, dissolved ^{129}Xe in lung tissue plasma (TP) and red blood cells (RBC) combined with a 3D radial trajectory was implemented within a 14s breath-hold.

Results: Results show an excellent chemical shift separation of the dissolved ^{129}Xe compartments and gas contamination removal, confirmed by a strong agreement between average imaging and global spectroscopy RBC/TP ratio measurements. Subjects with IPF exhibited reduced imaging gas transfer when compared to healthy volunteers. A significant increase of the amplitude of RBC signal cardiogenic oscillation was also observed. In IPF subjects, $DL_{CO}\%$ predicted was significantly correlated with RBC/TP and RBC/GAS ratios and the correlations were stronger in the inferior and periphery sections of the lungs.

Conclusion: Lung MRI of dissolved ^{129}Xe was performed with a 4-echo spectroscopic imaging method. Subjects with idiopathic pulmonary fibrosis demonstrated reduced xenon imaging gas transfer and increased cardiogenic modulation of dissolved xenon signal in the RBCs when compared to healthy volunteers.

Keywords: hyperpolarized ^{129}Xe, Lung, IPF, spectroscopic imaging

Introduction

Idiopathic Pulmonary Fibrosis (IPF) is a pulmonary disease of gas exchange and making the correct prognosis remains challenging due to a lack of sensitive biomarkers. It has no clear origin, affects mostly those over fifty years of age, causes fibrosis of the lung parenchyma and is rapidly progressive but unpredictable (1). Subjects with IPF present reduced gas exchange and therefore breathing difficulty during exercise, often associated with increased interstitial thickness. IPF progression is usually assessed via pulmonary function tests (PFTs) showing restriction of lung volumes measured by the forced vital capacity (FVC), reduced forced expiratory volume in 1s (FEV_1) on spirometry and reduction in lung gas transfer efficiency that can be estimated with the diffusion capacity of the lung for carbon monoxide (DL_{CO}). Those measurements are however insensitive to longitudinal change (2) and do not provide regional information about disease heterogeneity, thus new more sensitive biomarkers are required (3). MRI with hyperpolarized (HP) gases can be used to study regional changes in lung ventilation and microstructure (4). The solubility of HP ^{129}Xe gas in lung tissues and blood is of particular interest for the assessment of gas exchange (5,6) as dissolved ^{129}Xe exhibits two distinct resonance peaks corresponding to ^{129}Xe dissolved in lung tissue/plasma (TP, ~197 ppm relative to ^{129}Xe gas) and red blood cells (RBC, ~217 ppm). In IPF, spectroscopic measurements of ^{129}Xe dissolved phase uptake such as the RBC/TP ratio have been shown to be sensitive to gas transfer impairment and correlate well with disease severity (7,8). Additionally, this measurement has shown good reproducibility and is sensitive to disease progression over a 12-month period (3). More recently, it has been shown that; dissolved xenon RBC chemical shift (CS) is dependent on blood oxygenation level (9), which is significantly different in subjects with IPF when compared to controls (10), that the tissue/plasma barrier signal could be made of two distinct peaks (10), and that the magnitude of cardiogenic oscillations of the RBC signal amplitude observed during dynamic spectroscopic measurements is higher in subjects with IPF (11,12).

Imaging dissolved-phase ^{129}Xe remains challenging as it represents only 1-2% of the total magnetization of the gas-phase ^{129}Xe signal in the airways, and has a short transverse relaxation time T_2^* (~2 and 1 ms at 1.5T and 3T respectively). Ultra-short T_E sequences using radial (13) or spiral (14) k-space trajectories can help overcome this limitation. To perform CS separation and enable simultaneous imaging of ^{129}Xe in its different dissolved phase compartments, several strategies can be applied. Conventional phase-encoded chemical shift imaging has been applied to dissolved ^{129}Xe imaging of gas exchange in a pre-clinical setting (15), however long acquisition times have prevented successful application in human studies to date. The 1-point Dixon technique has been the most commonly used method in human studies to date (16). It requires a separate spectroscopic calibration acquisition performed at different echo times to derive the TE for which the TP and RBC signal have a 90-degree phase shift, since this value varies between subjects. This technique has been combined with image processing to display maps of the gas, TP and RBC signal ratios and compare the distribution of

RBC/TP ratios between healthy volunteers and subjects with IPF (17), and it has shown a good reproducibility in healthy subjects within one month (18). Another challenge in performing dissolved ^{129}Xe imaging is to design highly selective RF pulses with minimal off-resonant excitation of the gas phase (19). Due to imperfection of pulse design, residual gas signal contamination of a similar order of magnitude as the dissolved signal is usually observed and recently, the 1-point Dixon technique was modified to acquire a second echo time in order to perform gas phase signal contamination estimation and removal (20). However, the main limitation of the 1-point Dixon technique is the assumption that the k-space is acquired instantly at time TE and thus first-order phase evolution between the RBC and TP compartments during the acquisition readout time is neglected. With commonly used bandwidths (e.g. ~ 16 kHz) and a reported chemical shift value of 20 ppm, it can be estimated that a phase shift of approximately 10° occurs during the acquisition of each k-space point, which results in significant mixing of the different compartments' signals away from the center of k-space and hence image blurring. Moreover, the 1-point Dixon technique would be ill-conditioned for the reliable detection of a second dissolved peak in the TP signal as previously suggested (10).

More advanced multi-point Dixon or iterative decomposition of water and fat with echo asymmetry and least-squares estimation (IDEAL) (21) CS separation techniques are therefore advisable. A 3-point IDEAL 3D radial implementation has been used for dissolved xenon (22) and applied in populations of healthy volunteers and subjects with COPD and asthma (23), showing a significantly lower RBC/TP ratio in subjects with COPD and a good correlation with DL_{CO}. The efficient acquisition of the 3 radial echoes in one TR made the 3D acquisition short enough to fit in a single breath-hold, but it was assumed that there was no gas contamination, the T_2* for RBC and TP compartments was the same and k-space acquisition was instantaneous, by performing the CS separation in the image domain. Brodsky et al (24) proposed a signal model for IDEAL reconstruction which takes into account the additional phase accumulated by off-resonant spins at each point in the k-space acquisition trajectory. It has been applied to dissolved ^{129}Xe imaging with a spiral trajectory to measure xenon gas transfer dynamics with multiple TRs (25) and to perform CSSR imaging in healthy subjects (26). More recently, Kammerman et al. (27) proposed a more extensive model-based reconstruction of the IDEAL method, using a 4-point spectroscopic imaging technique similar to the one presented in this paper and integrating estimates of T_2^*, frequency shifts and field inhomogeneity maps, showing that the transverse relaxation rate of dissolved-phase ^{129}Xe can be a biomarker of lung injury in IPF.

In this work, a 4-point spectroscopic imaging technique with k-space decomposition of gas, TP and RBC signals via chemical-shift modeling combined with a 3D radial trajectory, is presented. By acquiring data at 4 different TEs, the gas phase signal contamination in the dissolved interleave can be modelled during the CS reconstruction and removed. The implementation of a radial trajectory also allows to sample rapidly the k-space center for each compartment and therefore investigation into the existence and amplitude of cardiogenic oscillations (9,11). This is a promising and complementary

addition for dissolved ^{129}Xe imaging, enabling the distinction between different cardiopulmonary phenotypes (28). While this usually requires a separate dynamic spectroscopic acquisition, in the proposed implementation we combine both acquisitions in a single breath-hold. The proposed method is evaluated in healthy volunteers and patients with IPF and imaging outcomes are compared with pulmonary function tests in patients.

Theory

The methodology for CS imaging of ^{129}Xe gas/dissolved compartments follows the chemical-shift modeling applied previously to ^{13}C metabolic imaging (29) but with the implementation of a 3D radial echo-planar spectroscopic imaging (EPSI) k-space trajectory to acquire the 4 TE_m data (m=1 to 4). The main equations of the signal modelling are recalled here for the HP ^{129}Xe signal consisting of three main compartments q of airspaces, tissue/plasma and RBC. The signal acquired $y_{m,n}$ of the nth k-space sample location $\mathbf{k}_n$ at the time after excitation $\tau_{m,n} = TE_m + t_n$, can be expressed after discretization of the spectral resonance frequencies ω_q and spatial dimension $\mathbf{r}_p$ as:

$$y_{m,n} = \sum_{p,q} e^{i\mathbf{k}_n \mathbf{r}_p} e^{i(\omega_q - 1/T_{2,q}^*)\tau_{m,n}} x_q(\mathbf{r}_p)$$

[1]

where $x_q(\mathbf{r})$ represents the distribution of the different resonances in image space. This model omits the regional magnetic field inhomogeneities that can cause additional, regionally varying frequency shifts in the measured signal and the decrease of longitudinal magnetization due to T_1 relaxation and RF-induced decay. It is possible to make a further few simplifications such as obtaining an estimate from a separate calibration spectrum of the resonance frequencies ω_q and $T_{2,q}^*$ values of each component. After accounting for the T_2^* decay only between echo times but not during the acquisition time of each echo, the following expression for the k-space signal is obtained:

$$y_{m,n} = \sum_q E_{m,q} e^{i\omega_q t_n} \xi_q(\mathbf{k}_n)$$

[2]

with: $\xi_q(\mathbf{k}_n) = \sum_p e^{i\mathbf{k}_n \mathbf{r}_p} x_q(\mathbf{r}_p)$ and $E_{m,q} = e^{i(\omega_q - 1/T_{2,q}^*)TE_m}$

where $\xi_q(\mathbf{k}_n)$ represents the distribution of the different resonances in k-space.

The CSI reconstruction consists of a two steps process:

i. matrix inversion of the preconditioned CS encoding matrix E to reconstruct each $\xi_q(\mathbf{k}_n)$ in k-space (where † denotes the Moore–Penrose pseudo-inverse):
$$\xi_q(\mathbf{k}_n) = e^{-i\omega_q t_n} (E^\dagger y_n)_q$$

4

[3]

    ii.   using gridding (30) to reconstruct images of each compartment spatially.

Moreover, the effective number of signal averages (NSA) approach (31) that depends on the conditioning of E can be used to optimize the echo time spacing ΔTE in order to minimize the noise amplification during the CS inversion of Eq. [3]:

$$NSA_q = \frac{1}{(E^H E)_{q,q}^{-1}}$$

[4]

where H denotes the complex conjugate transpose.

Methods

Subject recruitment and PFTs

All imaging protocols were performed under the approval of the UK national research ethics committee. 10 healthy volunteers (HV) with no known respiratory conditions, and 25 patients with a clinical diagnosis of IPF were recruited and provided written informed consent. The diagnosis of IPF was established by a multi-disciplinary team at a single tertiary interstitial lung disease center. IPF subjects underwent pulmonary function tests on the same day as the MRI visit, including FVC, FEV_1 and DL_{CO}. Percent predicted values were calculated using Global Lung Initiative reference values in accordance with usual clinical practice (32). Subject demographics are presented in Table 1.

MRI acquisition

All imaging was performed on a 1.5T GE HDx scanner with HP ^{129}Xe polarized to ~30% polarization and produced by a home-built flow mode spin exchange optical pumping polarizer at a production rate of 1L in 18 min (33). Using the effective number of signal averages approach (see Fig. 1.a and above Theory section), an optimum ΔTE of 0.7 ms was chosen such that a flyback implementation of 4 TEs (1st TE ~ 0.55 ms from the center position of the RF pulse) could be performed during the same TR (radial EPSI, see Fig. 1.b) in order to minimize the number of RF pulses applied, keep the readout length of the same order of magnitude as the dissolved xenon T_2^* and keep the total duration within a practical breath-hold time. A spoiled interleaved RF excitation of gaseous and dissolved-phase ^{129}Xe (FA= 0.7/40°, respectively with RF frequency centered on the TP peak for the dissolved xenon interleave) was implemented. A 0.8ms composite RF pulse with amplitude modulation, optimized previously for minimizing off-resonance excitation (19), was used. The 3D half-echo radial sequence had 332 projections (uniform sampling with random ordering, 10% oversampling in the radial readout direction, 11 data points acquired per echo time and 4-fold radial under-sampling at k max), 2 cm isotropic voxel

(FOV=40cm, BW=31.25kHz, 14s breath-hold acquisition, 1L of HP ^{129}Xe) and a TR of 20ms. The TR is here defined as the time interval between the gas and dissolved xenon interleaves. 20 dummy RF pulses (10 on gas and 10 on dissolved xenon) were implemented at the start of the sequence to deplete the magnetization that was originally present in the blood in the pulmonary veins. A whole-lung spectrum (BW=8kHz, 512pts, 200 averages, TR=74ms, 22° flip angle) was acquired with a 600mL dose of ^{129}Xe prior to imaging to improve reconstruction by providing accurate determination of the respective ^{129}Xe resonance frequencies as previously described (29).

Figure 1 – here

Data analysis:

The gaseous ^{129}Xe interleave images were produced with a standard 3D radial reconstruction using the optimal Kaiser-Bessel convolution kernel formula from (30) for a minimal oversampling of 1.1 and a kernel width of 8. A triple Lorentzian fit of the calibration spectroscopy data in the frequency domain was performed similarly as in (7) to derive patient specific resonance frequencies and T_2* values of each peaks. For the dissolved ^{129}Xe interleave data, the same reconstruction was applied after performing chemical shift separation in k-space. Due to inconsistent off-resonant excitation of the gas phase in the dissolved interleave, the gas images produced from that interleave were only assessed and compared qualitatively to the gas interleave image and later discarded. After deriving a region of interest on the TP image (threshold based using SNR>5) and correcting for subject specific differences in T_2* derived from the calibration spectrum, ratio maps of RBC/TP, TP/GAS and RBC/GAS were produced (Fig. 2). Global and regional averages (anterior/posterior, center/outer, inferior/middle/superior parts of the lungs) were derived for each subject. To derive the center (core) and outer (peel) regions of the lungs, an ellipsoid centered at the center of mass of the lung mask was created with radii in three directions defined as 0.79 time the original full mask radii. The value of 0.79 was chosen as it would correspond to half the volume of the original mask in the case of a sphere or an ellipsoid ($0.79 \sim 0.5^{1/3}$) aiming to obtain two zones of similar volumes.

Figure 2 – here

With the chosen radial encoding scheme, the center of k-space for each compartment was sampled every 40 ms (2 x TR), enabling the observation of the dissolved ^{129}Xe signal decay during breath-hold and also the periodic RBC signal oscillations due to the cardiac cycle (11). The peak-to-peak amplitude of these cardiogenic oscillations was calculated from the first half of the data where the SNR is sufficiently high by performing a band pass filtering (0.5 to 2.5Hz) and an automatic peak detection on the T1 decay corrected signal evolution of the RBC k-space center data after CS separation (Figure 3). All CS separation and data reconstruction were implemented in-house using MATLAB (MathWorks, Natick, Massachusetts, USA).

6

Figure 3 – here

Statistical methods:

Spearman's rank correlation coefficient was used to assess similarities between the global RBC/TP ratio from spectroscopy and imaging sequences whereas Pearson's rank correlation coefficient was used to assess the strength of correlation between PFTs and imaging metrics. Paired t-tests and one-way ANOVA were used to assess regional differences (anterior/posterior, center/outer, inferior/middle/superior parts of the lungs) of signal distribution and average ratio within each group. Unpaired t-tests were used to test for significant differences in RBC amplitude oscillations, and global and regional dissolved ^{129}Xe imaging ratios between HV and IPF subjects. All statistical analyses were performed using GraphPad Prism (San Diego, USA), and statistical significance level was set at *P*<0.05.

Results

Statistics of the study population are summarized in Table 1. With a mean [min, max] predicted DL_{CO}% of 71% [31%, 101%], the IPF cohort can be considered as mild on average but with a wide spread of disease severity. From the calibration spectroscopy data, the average TP and RBC chemical shifts from the gas resonance in healthy volunteers and IPF subjects groups are presented in Table 1 together with the average T_2^* values for each compartment. The quality of the CS modeling reconstruction was assessed by comparing gas ventilation images from the gas excited interleave with gas contamination images from the dissolved ^{129}Xe interleave. In all cases, the ventilation distributions inside the lungs of ^{129}Xe gas were equivalent with an average (±SD) pixel by pixel correlation of the signal intensity of r=0.93±0.03 over the entire IPF population. A representative example of a quantitative pixel by pixel correlation of normalized ventilation between the two images and a Bland-Altman analysis is displayed in Figure 4.a & 4.b. By comparing the average signal intensity in both non-normalized images, it is also possible to infer a flip angle corresponding to the off-resonance excitation in the dissolved interleave data. The ratio of the gas signal between the dissolved and gas interleave data was found to be 0.15±0.02, which corresponds to a 0.1° flip angle for off resonance gas excitation. A high correlation was found between the global RBC/TP ratio derived from imaging and the ratio derived from whole-lung calibration spectroscopy (Figure 4.c, r=0.90, p <0.0001), demonstrating further that the CS modeling reconstruction and subsequent production of 3D maps of TP and RBC uptake in the lung was successful.

Figure 4 – here

In both HV and IPF groups, RBC and TP mean signals were higher in the dependent (posterior) part of the lung (p<0.0001) as observed previously (13). The mean gas signal however was not significantly different (anterior/posterior: p=0.18 for HV and p=0.27 in IPF). The ventilation was also preferably distributed in the inferior part of the lung (p=0.02 for HV and p=0.0003 for IPF) and so was the

dissolved ^{129}Xe in TP (p=0.0003 for HV and p<0.0001 in IPF). Looking at the barrier uptake (TP/GAS ratio), it was significantly higher in the dependent part of the lung (p=0.0006 for HV and p<0.0001 in IPF, Fig. 5.a & 5.b). The RBC gas transfer (RBC/GAS ratio) was also significantly higher in the posterior part (p=0.0009 for HV and p=0.0002 in IPF, Fig. 5.c & 5.d) and lower in the lung periphery (peel) than in the core, with p=0.002 for HV and p=0.02 in IPF subjects (see Fig. 5.e & 5.f). Regarding the RBC/TP ratio, there were no significant differences in anterior/posterior values in both groups. However, RBC/TP ratio was lower in the inferior part (p=0.02 for HV and p=0.0003 in IPF).

Figure 5 – here

When comparing HV and IPF groups, the average imaging RBC/TP and RBC/GAS ratios were significantly lower in subjects with IPF (Figure 5), with average values in HV of 0.47 and 0.22 in IPF (p<0.0001) for RBC/TP and 3.6 x 10^{-3} and 1.9 x 10^{-3} (p=0.002) for RBC/GAS respectively. But no significant difference was observed in TP/GAS ratio (average values of 7.5 x 10^{-3} and 8.3 x 10^{-3}, p=0.20). Cardiogenic oscillations were observed in the time evolution of the RBC signal only (see example in Fig. 3) and the amplitude of the oscillations was significantly higher in subjects with IPF when compared to healthy volunteers (Figure 5.d, HV: 12.8 % and IPF: 18.8 % respectively, p=0.001).

Figure 6 – here

In the IPF cohort, DL_{CO}% was significantly correlated with the whole-lung (global) RBC/TP ratio (r=0.60, p=0.002) and all mean regional ratios, but the correlations were stronger in the inferior (r=0.66, p=0.0004), posterior (r=0.62, p=0.0009) and peripheral parts of the lungs (r=0.63, p=0.0007) (see Figure 6). Similarly, DL_{CO}% correlated with global (r=0.53, p=0.007) and regional RBC/GAS ratios and the correlations were stronger in the inferior (r=0.62, p=0.001) and posterior parts of the lung (r=0.57, p=0.003). Center and outer parts of the lungs had a similar correlation as the global RBC/GAS ratio. No significant correlation was observed between TP/GAS ratios and DL_{CO}% or between any imaging metrics and FVC% or FEV1%. The amplitude of the cardiogenic oscillations was not significantly correlated with DL_{CO}% (r=-0.33, p=0.11).

Figure 7 – here

To assess the sensitivity of the chemical shift separation and derived average imaging ratios to the subject specific measurements of the T_2^* and peak frequencies, an additional analysis of the IPF cohort data was performed taking the average values presented in Table 1 for the reconstruction of each data set. The mean absolute error on global RBC/TP, TP/GAS and RBC/GAS ratios was found to be 2.0 ± 1.3 % , 2.6 ± 1.8 % and 3.5 ± 2.8 % respectively. The new correlation of the global RBC/TP and RBC/GAS imaging ratios with DL_{CO}% were slightly lower with a correlation coefficient r of 0.55 (p=0.004) and 0.49 (p=0.01) respectively.

Discussion

We have presented an implementation of echo-planar spectroscopic imaging for dissolved HP [129]Xe in the lung. Whereas other methods are usually empirically validated against clinical findings only, here we assessed and validated the performance of the CS separation by three different approaches: (i) a good agreement between the gas contamination from the dissolved [129]Xe interleave and the gas ventilation image, (ii) the observation of cardiogenic oscillations at the k-space center for the RBC data, and (iii) a high correlation between the average imaging RBC/TP ratio and the ratio from whole-lung spectroscopy. It is worth noting that for the 1-point Dixon imaging technique (16,17), a calibration spectroscopic acquisition is required beforehand to calculate the RBC/TP ratio, which is used as prior knowledge to phase and align the RBC and TP signals on the real and imaginary channels of the receiver. Thus, global lung average ratio values are derived from assumptions made on the basis of results from a separate spectroscopic acquisition. However, in the present technique, the calibration spectroscopy sequence is only performed to derive patient specific resonance frequencies and T_2* values for each compartment. As demonstrated in the results, when compared with a reconstruction based on assuming representative values for the IPF population, this prior knowledge can increase the accuracy of the reconstruction by a few percent. Moreover, in future work, the measurement of this spectrum can be readily integrated as an additional projection during the imaging sequence, as originally performed in Wiesinger et al (29) to further reduce the number of xenon doses required and shorten the MR protocol. It is worth noting that in the protocol of this study, the spectroscopic calibration was also required to generate additional outputs that are not presented here but the implementation of dummy RF excitation with longer acquisition time at the start of the sequence has now been performed in our center to make it a standalone sequence.

The differences between the spectroscopic and imaging RBC/TP ratio values result from a difference in flip angle and TR values used for both sequences (22˚ and 74 ms when compared to 40˚ and 40 ms, respectively). With an almost twice longer TR for the global spectroscopic sequence, the amount of xenon blood uptake is higher and RBC/TP ratios are on average 10.9 % higher (see Fig. 4.c) consistent with previous CSSR spectroscopic studies (5). With average RBC/TP values of 0.47 and 0.22 for HV and subjects with IPF respectively, the results are in agreement with previously published data (0.55 and 0.16 in (7), 0.50 and 0.15 in (16), 0.58 and 0.21 in (17)) and the correlation with DL_{CO} confirms similar findings (7,17). This data supports our proposed 4-point spectroscopic imaging technique as a robust method for sensitive and non-invasive measurement of disease progression in patients with IPF. However, the elevated, but not statistically-significant increase, of TP/GAS ratio in subjects with IPF when compared to HV is different from previously reported results (wherein a clear significance was reported). With fibrosis resulting in thickening of the alveolar–capillary membrane, it can be expected to observe higher barrier uptake in addition to a reduced efficiency of xenon to transfer to capillary RBCs. A difference in disease severity in our IPF patient group when compared with other work (e.g.

average DL_{CO} % predicted of 71% in the present study when compared to 48% in (8) and (17)) coupled with the difference in imaging parameters may explain why a significant difference in TP/GAS was not observed in this work. However, our results are in line with those acquired with a similar acquisition strategy recently by Kammerman et al. (27) and for which the average DL_{CO}% predicted in the IPF subjects group was 56%.

Looking at the regional differences in HV and IPF subjects, the increased TP/GAS and RBC/GAS ratio in the dependent part of the lung is expected considering a higher density of tissue and capillaries due to gravity. In subjects with IPF, it is not surprising to observe a reduced imaging gas transfer in the inferior part of the lung and stronger correlations of imaging metrics with DL_{CO}% in inferior and outer parts of the lung, which can be explained by the predominantly basal and peripheral presentation of fibrosis. IPF is a spatially heterogeneous disease with normal lung tissue next to abnormal tissue. Producing images of regional gas exchange with dissolved xenon is therefore of great interest, providing regional insight into thickening of the alveolar interstitium, destruction of alveoli and capillary perfusion deficit. Additionally, cardiogenic oscillations of the dissolved ^{129}Xe signal in the RBCs have been successfully observed with this spectroscopic imaging method, without requiring a separate additional dynamic spectroscopy acquisition (28). It is worth noting that a new imaging method combining 1-point Dixon and keyhole image reconstruction techniques has been recently reported to achieve similar potential (34). Moreover, the significantly increased amplitude of these oscillations in the IPF subjects imaged agrees well with previous findings (11). It has been suggested that a reduced capillary blood volume in IPF with a cardiac output similar to HV would likely explain a higher percentage change of capillary blood volume during a cardiac cycle and therefore the percentage change of dissolved xenon in RBCs.

Monitoring decline/progression in IPF is complex. CT imaging correlates poorly with lung function and symptoms. Pulmonary function testing is subject to 10% FVC and 15% DL_{CO} inter-test variability. Interventions with anti-fibrotic therapies have consistently shown little effect on DL_{CO} measures. Many patients with IPF have concomitant respiratory disease such as COPD or emphysema. Determining the cause of a respiratory symptomatic deterioration, therefore, is complex as PFTs simply measure total lung parameters, with reduced gas transfer, for example, possibly being attributed to non IPF components of lung disease. As such the use of regional imaging can more clearly delineate pathological progression and may be useful both clinically and in future research studies.

One of the limitations of this study is that the healthy volunteers and subjects with IPF are not well age-matched and that, although IPF is dominantly a male disease, the female population is equally underrepresented in the healthy subjects and IPF patients. The study was also performed at 1.5T and it might be expected that a lower SNR (due to approximately twice shorter dissolved ^{129}Xe T_2* values) would be observed at 3T. However, with a readout time of only ~ 2ms for the first three echo times (the

fourth echo time mainly helps model the gas signal during the reconstruction), the method should be translatable to 3T, similar to what was shown recently for the 1-point Dixon method (35). Alternatively, using twice as many dissolved phase interleaves and acquiring only two of the 4 echo per interleave (1st and 3rd echoes for first interleave and 2nd and 4th for the second interleave) could be implemented using a shorter optimum ΔTE of 0.35 ms at 3T and keep the same number of radial projection and image resolution by shortening the flip angle and repetition time.

Since the 4-echo flyback radial acquisition strategy is similar to work recently published by Kammerman et al. (27), but the reconstruction approach used is different, a comparison of data analysis and results could be performed in future work to study the influence of optimizing the echo spacing on SNR and image artifact, evaluate the potential for T_2^* to be a biomarker in IPF and implement a B0 inhomogeneity correction iteratively. Results from that study seem to be well in line with our results in terms of average frequencies and T_2^* values estimation from spectroscopy data in both groups and global average ratios differences between groups. Similar significant correlations with $DL_{co}\%$ of the average RBC/TP and RBC/GAS ratios (but not for the TP/GAS ratio) were also found. It is worth noting that incorporating / not incorporating the chemical shifts and T_2^* decay rates in their model yielded similar distributions of regional ratios in the lungs and that the omission of more complex modeling features in our reconstruction might have a limited impact on the results.

Conclusions

A 4-echo 3D radial EPSI technique for dissolved ^{129}Xe imaging has been implemented and successfully validated against global lung spectroscopy measurements. Reduced regional gas transfer and higher cardiogenic oscillations were observed in patients with IPF when compared to healthy volunteers. The main advantage of the presented technique is the implementation of the chemical-shift modeling and separation in k-space. When performed in image space, the reconstruction assumes a singular echo time that may result in severe image blurring. Acquiring a higher number of echoes than the number of compartments also significantly improves peak separation, allowing clear gas phase contamination removal from the dissolved data. With the recent report of distinct xenon MRI signatures with diverse cardiopulmonary diseases (28), possible future applications could focus on longitudinal monitoring of IPF, early diagnosis of IPF, COPD and PAH and regional xenon gas transfer maps could provide complementary information to CT imaging.

Acknowledgements

References

1. King TE, Jr., Pardo A, Selman M. Idiopathic pulmonary fibrosis. Lancet 2011;378(9807):1949-1961.
2. Nathan SD, Albera C, Bradford WZ, Costabel U, du Bois RM, Fagan EA, Fishman RS, Glaspole I, Glassberg MK, Glasscock KF, King TE, Jr., Lancaster L, Lederer DJ, Lin Z, Pereira CA, Swigris JJ, Valeyre D, Noble PW, Wells AU. Effect of continued treatment with pirfenidone following clinically meaningful declines in forced vital capacity: analysis of data from three phase 3 trials in patients with idiopathic pulmonary fibrosis. Thorax 2016;71(5):429-435.
3. Weatherley ND, Stewart NJ, Chan HF, Austin M, Smith LJ, Collier G, Rao M, Marshall H, Norquay G, Renshaw SA, Bianchi SM, Wild JM. Hyperpolarised xenon magnetic resonance spectroscopy for the longitudinal assessment of changes in gas diffusion in IPF. Thorax 2019;74(5):500-502.
4. Fain SB, Korosec FR, Holmes JH, O'Halloran R, Sorkness RL, Grist TM. Functional lung imaging using hyperpolarized gas MRI. J Magn Reson Imaging 2007;25(5):910-923.
5. Stewart NJ, Leung G, Norquay G, Marshall H, Parra-Robles J, Murphy PS, Schulte RF, Elliot C, Condliffe R, Griffiths PD, Kiely DG, Whyte MK, Wolber J, Wild JM. Experimental validation of the hyperpolarized (129) Xe chemical shift saturation recovery technique in healthy volunteers and subjects with interstitial lung disease. Magn Reson Med 2015;74(1):196-207.
6. Mugler JP, 3rd, Altes TA, Ruset IC, Dregely IM, Mata JF, Miller GW, Ketel S, Ketel J, Hersman FW, Ruppert K. Simultaneous magnetic resonance imaging of ventilation distribution and gas uptake in the human lung using hyperpolarized xenon-129. Proc Natl Acad Sci U S A 2010;107(50):21707-21712.
7. Kaushik SS, Freeman MS, Yoon SW, Liljeroth MG, Stiles JV, Roos JE, Foster W, Rackley CR, McAdams HP, Driehuys B. Measuring diffusion limitation with a perfusion-limited gas--hyperpolarized 129Xe gas-transfer spectroscopy in patients with idiopathic pulmonary fibrosis. J Appl Physiol 2014;117(6):577-585.
8. Wang JM, Robertson SH, Wang Z, He M, Virgincar RS, Schrank GM, Smigla RM, O'Riordan TG, Sundy J, Ebner L, Rackley CR, McAdams P, Driehuys B. Using hyperpolarized 129Xe MRI to quantify regional gas transfer in idiopathic pulmonary fibrosis. Thorax 2017.
9. Norquay G, Leung G, Stewart NJ, Wolber J, Wild JM. (129) Xe chemical shift in human blood and pulmonary blood oxygenation measurement in humans using hyperpolarized (129) Xe NMR. Magn Reson Med 2017;77(4):1399-1408.
10. Robertson SH, Virgincar RS, Bier EA, He M, Schrank GM, Smigla RM, Rackley C, McAdams HP, Driehuys B. Uncovering a third dissolved-phase (129) Xe resonance in the human lung: Quantifying spectroscopic features in healthy subjects and patients with idiopathic pulmonary fibrosis. Magn Reson Med 2017;78(4):1306-1315.
11. Bier EA, Robertson SH, Schrank GM, Rackley C, Mammarappallil JG, Rajagopal S, McAdams HP, Driehuys B. A protocol for quantifying cardiogenic oscillations in dynamic (129) Xe gas exchange spectroscopy: The effects of idiopathic pulmonary fibrosis. NMR Biomed 2019;32(1):e4029.
12. Ruppert K, Altes TA, Mata JF, Ruset IC, Hersman FW, Mugler JP, 3rd. Detecting pulmonary capillary blood pulsations using hyperpolarized xenon-129 chemical shift saturation recovery (CSSR) MR spectroscopy. Magn Reson Med 2016;75(4):1771-1780.
13. Kaushik SS, Freeman MS, Cleveland ZI, Davies J, Stiles J, Virgincar RS, Robertson SH, He M, Kelly KT, Foster WM, McAdams HP, Driehuys B. Probing the regional distribution of pulmonary gas exchange through single-breath gas- and dissolved-phase 129Xe MR imaging. J Appl Physiol 2013;115(6):850-860.
14. Doganay O, Wade T, Hegarty E, McKenzie C, Schulte RF, Santyr GE. Hyperpolarized (129) Xe imaging of the rat lung using spiral IDEAL. Magn Reson Med 2016;76(2):566-576.
15. Swanson SD, Rosen MS, Coulter KP, Welsh RC, Chupp TE. Distribution and dynamics of laser-polarized (129)Xe magnetization in vivo. Magn Reson Med 1999;42(6):1137-1145.

16. Kaushik SS, Robertson SH, Freeman MS, He M, Kelly KT, Roos JE, Rackley CR, Foster WM, McAdams HP, Driehuys B. Single-breath clinical imaging of hyperpolarized (129)Xe in the airspaces, barrier, and red blood cells using an interleaved 3D radial 1-point Dixon acquisition. Magn Reson Med 2016;75(4):1434-1443.

17. Wang Z, Robertson SH, Wang J, He M, Virgincar RS, Schrank GM, Bier EA, Rajagopal S, Huang YC, O'Riordan TG, Rackley CR, McAdams HP, Driehuys B. Quantitative analysis of hyperpolarized (129) Xe gas transfer MRI. Med Phys 2017;44(6):2415-2428.

18. Hahn AD, Kammerman J, Evans M, Zha W, Cadman RV, Meyer K, Sandbo N, Fain SB. Repeatability of regional pulmonary functional metrics of Hyperpolarized (129) Xe dissolved-phase MRI. J Magn Reson Imaging 2019;50(4):1182-1190.

19. Leung G, Norquay G, Schulte RF, Wild JM. Radiofrequency pulse design for the selective excitation of dissolved 129Xe. Magn Reson Med 2015;73(1):21-30.

20. Hahn AD, Kammerman J, Fain SB. Removal of hyperpolarized (129) Xe gas-phase contamination in spectroscopic imaging of the lungs. Magn Reson Med 2018;80(6):2586-2597.

21. Reeder SB, Pineda AR, Wen Z, Shimakawa A, Yu H, Brittain JH, Gold GE, Beaulieu CH, Pelc NJ. Iterative decomposition of water and fat with echo asymmetry and least-squares estimation (IDEAL): application with fast spin-echo imaging. Magn Reson Med 2005;54(3):636-644.

22. Qing K, Ruppert K, Jiang Y, Mata JF, Miller GW, Shim YM, Wang C, Ruset IC, Hersman FW, Altes TA, Mugler JP, 3rd. Regional mapping of gas uptake by blood and tissue in the human lung using hyperpolarized xenon-129 MRI. J Magn Reson Imaging 2014;39(2):346-359.

23. Qing K, Mugler JP, 3rd, Altes TA, Jiang Y, Mata JF, Miller GW, Ruset IC, Hersman FW, Ruppert K. Assessment of lung function in asthma and COPD using hyperpolarized 129Xe chemical shift saturation recovery spectroscopy and dissolved-phase MRI. NMR Biomed 2014;27(12):1490-1501.

24. Brodsky EK, Holmes JH, Yu H, Reeder SB. Generalized k-space decomposition with chemical shift correction for non-Cartesian water-fat imaging. Magn Reson Med 2008;59(5):1151-1164.

25. Doganay O, Chen M, Matin T, Rigolli M, Phillips JA, McIntyre A, Gleeson FV. Magnetic resonance imaging of the time course of hyperpolarized (129)Xe gas exchange in the human lungs and heart. Eur Radiol 2019;29(5):2283-2292.

26. Zanette B, Santyr G. Accelerated interleaved spiral-IDEAL imaging of hyperpolarized (129) Xe for parametric gas exchange mapping in humans. Magn Reson Med 2019;82(3):1113-1119.

27. Kammerman J, Hahn AD, Cadman RV, Malkus A, Mummy D, Fain SB. Transverse relaxation rates of pulmonary dissolved-phase Hyperpolarized (129) Xe as a biomarker of lung injury in idiopathic pulmonary fibrosis. Magn Reson Med 2020;84(4):1857-1867.

28. Wang Z, Bier EA, Swaminathan A, Parikh K, Nouls J, He M, Mammarappallil JG, Luo S, Driehuys B, Rajagopal S. Diverse cardiopulmonary diseases are associated with distinct xenon magnetic resonance imaging signatures. Eur Respir J 2019;54(6).

29. Wiesinger F, Weidl E, Menzel MI, Janich MA, Khegai O, Glaser SJ, Haase A, Schwaiger M, Schulte RF. IDEAL spiral CSI for dynamic metabolic MR imaging of hyperpolarized [1-13C]pyruvate. Magn Reson Med 2012;68(1):8-16.

30. Beatty PJ, Nishimura DG, Pauly JM. Rapid gridding reconstruction with a minimal oversampling ratio. IEEE Trans Med Imaging 2005;24(6):799-808.

31. Reeder SB, Brittain JH, Grist TM, Yen YF. Least-squares chemical shift separation for (13)C metabolic imaging. J Magn Reson Imaging 2007;26(4):1145-1152.

32. Quanjer PH, Stanojevic S, Cole TJ, Baur X, Hall GL, Culver BH, Enright PL, Hankinson JL, Ip MSM, Zheng J, Stocks J, Stocks J, Baur X, Hall GL, Culver B, Quanjer PH, Stanojevic S, Cole TJ, Stocks J, Hankinson JL, Enright PL, Zheng J, Ip MSM, Schindler C. Multi-ethnic reference values for spirometry for the 3–95-yr age range: the global lung function 2012 equations. Eur Respir J 2012;40(6):1324-1343.

33. Norquay G, Collier GJ, Rao M, Stewart NJ, Wild JM. 129Xe-Rb Spin-Exchange Optical Pumping with High Photon Efficiency. Physical Review Letters 2018;121(15):153201.

34. Niedbalski PJ, Bier EA, Wang Z, Willmering MM, Driehuys B, Cleveland ZI. Mapping cardiopulmonary dynamics within the microvasculature of the lungs using dissolved (129)Xe MRI. J Appl Physiol 2020;129(2):218-229.

35.   Wang Z, He M, Bier E, Rankine L, Schrank G, Rajagopal S, Huang YC, Kelsey C, Womack S, Mammarappallil J, Driehuys B. Hyperpolarized (129) Xe gas transfer MRI: the transition from 1.5T to 3T. Magn Reson Med 2018;80(6):2374-2383.

Tables:

Table 1:
Demographics and spectral properties of HP ^{129}Xe from the spectroscopic calibration

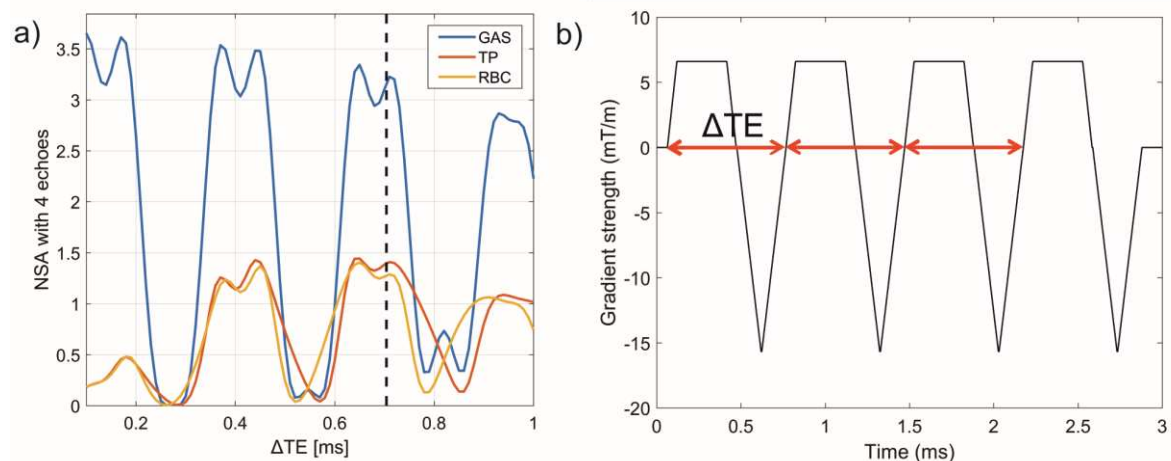|	**Healthy Volunteers**	**IPF**
Subjects	10	25
Female/Male	2/8	4/21
Age (median [min, max])	38yrs [25, 65]	74yrs [53, 80]
FVC % predicted (mean ± SD)	-	91% ± 16%
DL$_{CO}$ % predicted (mean ± SD)	-	71% ± 16%
FEV1 % predicted (mean ± SD)	-	88% ± 15%
TP chemical shift in ppm	197.9 ± 0.3	197.5 ± 0.3
RBC chemical shift in ppm	216.9 ± 0.6	215.7 ± 0.9
Gas T$_2$* in ms	14.2 ± 2.6	12.8 ± 2.4
TP T$_2$* in ms	2.18 ± 0.06	2.4 ± 0.1
RBC T$_2$* in ms	1.89 ± 0.05	2.3 ± 0.2

Figure captions:

Figure 1: a) Effective NSA as a function of the value of the echo time spacing ΔTE for 4 echo times. Simulations were performed assuming frequency values of -3.5 kHz for gas, 0 Hz for TP and 330 Hz for RBC at 1.5 T and T$_2$* values of 20, 2.1 and 1.9 ms, respectively. A ΔTE value of 0.7 ms (dashed vertical line in a)) was chosen and implemented for the 3D half echo flyback radial trajectory whose corresponding absolute gradient strength during readout acquisition is displayed in b).
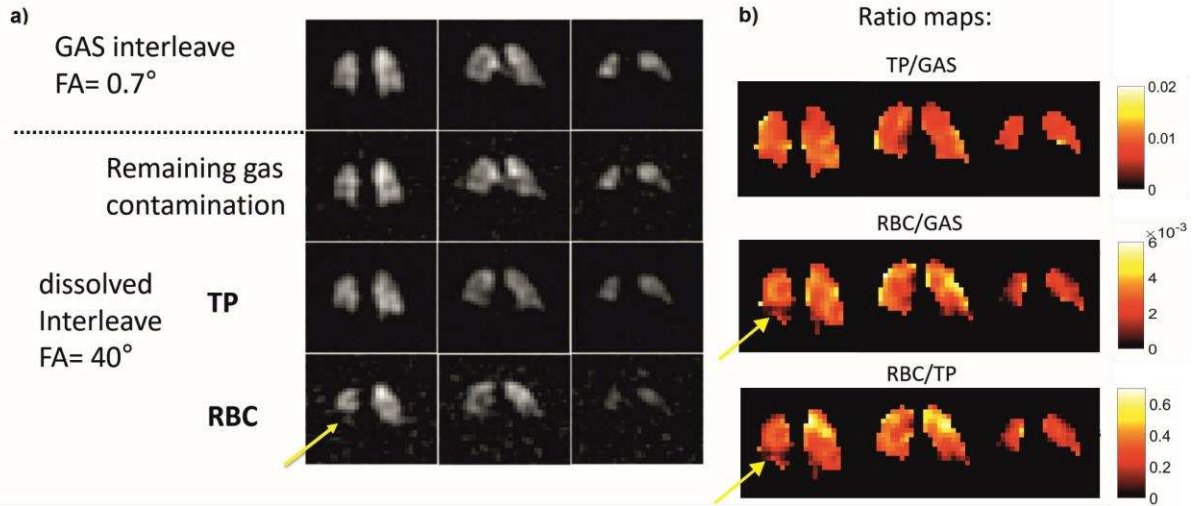
Figure 2: Example ^{129}Xe MR images and ratio maps in a subject with IPF with 1L of HP ^{129}Xe. a) Top: gas ventilation image after re-gridding and Fourier transform of the gas interleave data. Bottom: Gas, TP and RBC images of the same subject after EPSI reconstruction of the dissolved interleave 4 TE k-space data. Residual gas contamination from off resonance excitation can be observed and removed from dissolved phase data. b) Corresponding ratio maps after T_2^* and flip angle correction. The yellow arrows highlight a region of low xenon blood uptake, although normally ventilated.
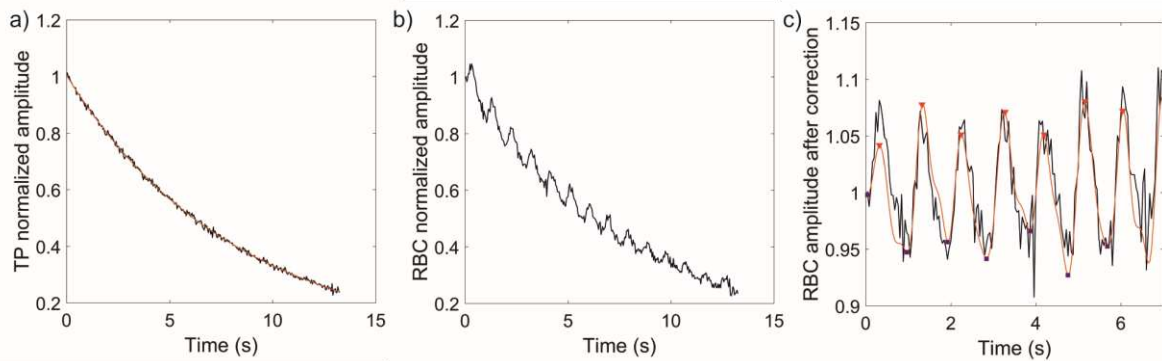
Figure 3: Normalized amplitudes of the TP (a) and RBC (b) signals (k-space center absolute values) with breath-hold time in a healthy volunteer. A bi-exponential fit of the TP decay (red line in a)) is used to correct the RBC signal: c) RBC signal after decay correction. After filtering (red line), a peak detection algorithm is used to detect maxima (red triangles) and minima (blue squares) and calculate an average peak to peak amplitude oscillation for RBC signal.
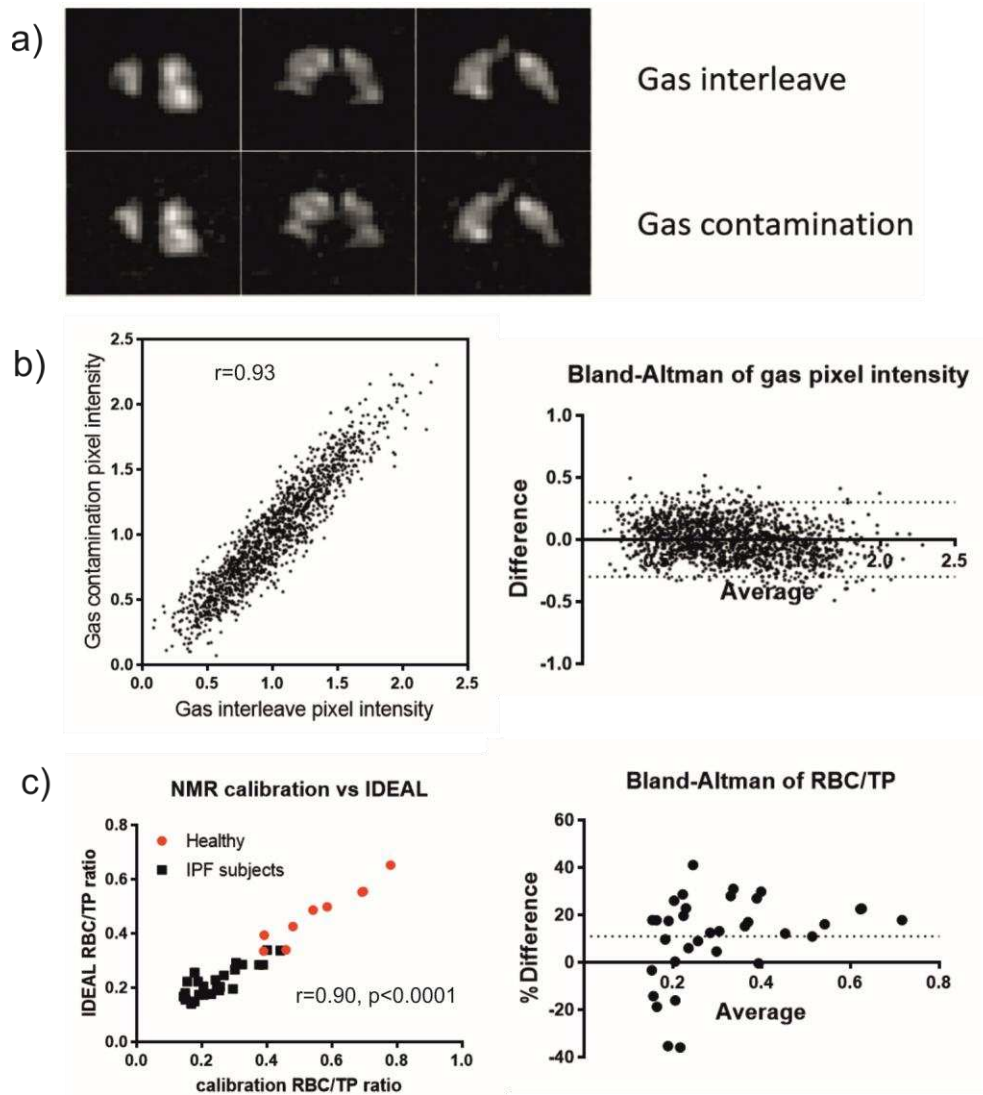
Figure 4: Validation of the imaging chemical shift separation and reconstruction method. a) Visual comparison of 3 coronal slices of the ^{129}Xe gas distribution in the lung of an IPF subject from the gas and dissolved interleave (gas contamination) data. b) Quantitative correlation and Bland-Altman analysis of the normalized pixel intensity of the gas images derived from gas and dissolved interleave data over the whole image in a representative subject (bias of 0; 95% limits of agreement: [-0.3, 0.3]). c) Validation of mean imaging RBC/TP ratio with whole-lung spectroscopy performed before imaging (correlation and Bland-Altman analysis, bias of 10.9 %).
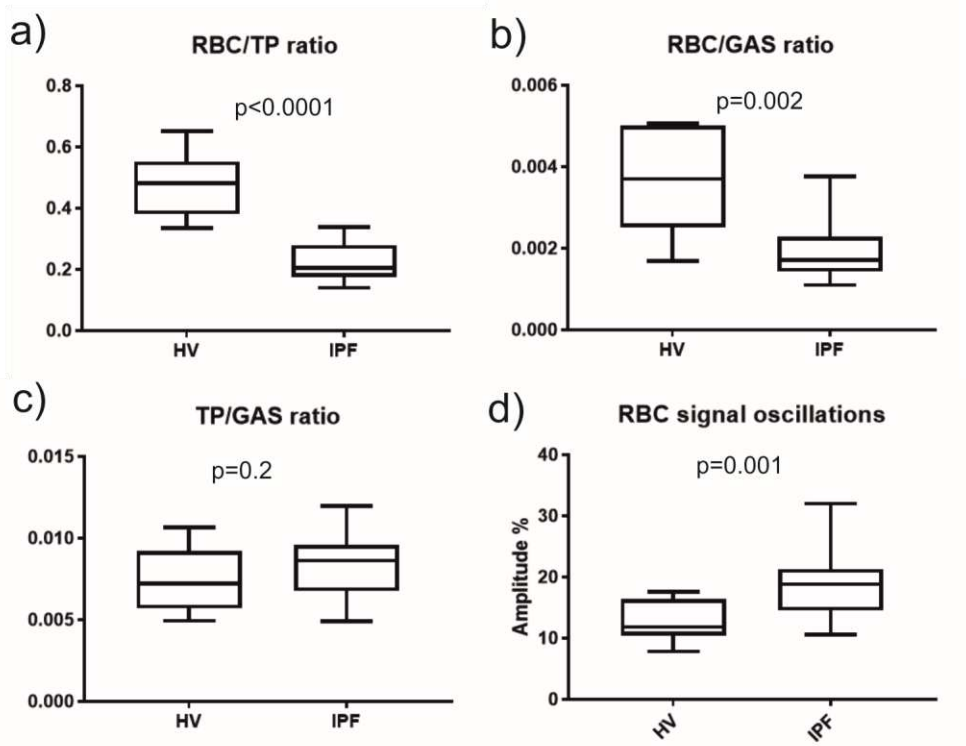
Figure 5: Comparison (Box plots) of significant difference in regional average ratio in HV (a), c) & e)) and IPF subjects (b), d) & f)).
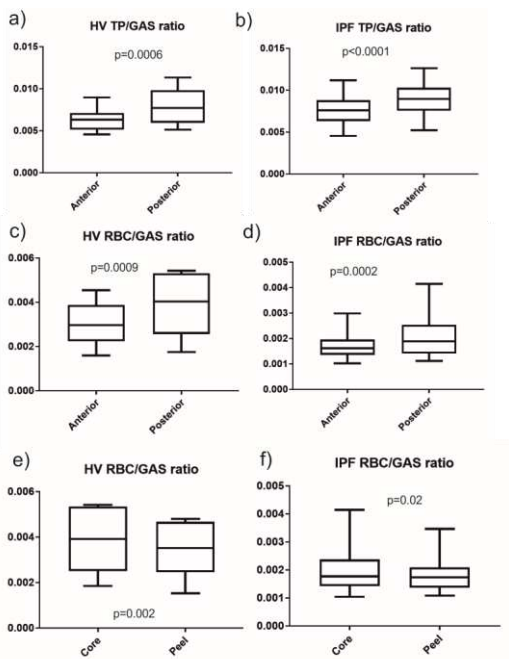

Figure 6: Box plots of RBC/TP (a), RBC/GAS (b), TP/GAS (c) and RBC amplitude oscillations (d) between healthy volunteers and subjects with IPF (unpaired t-test p<0.0001, p=0.002, p=0.20 and p=0.001 respectively).
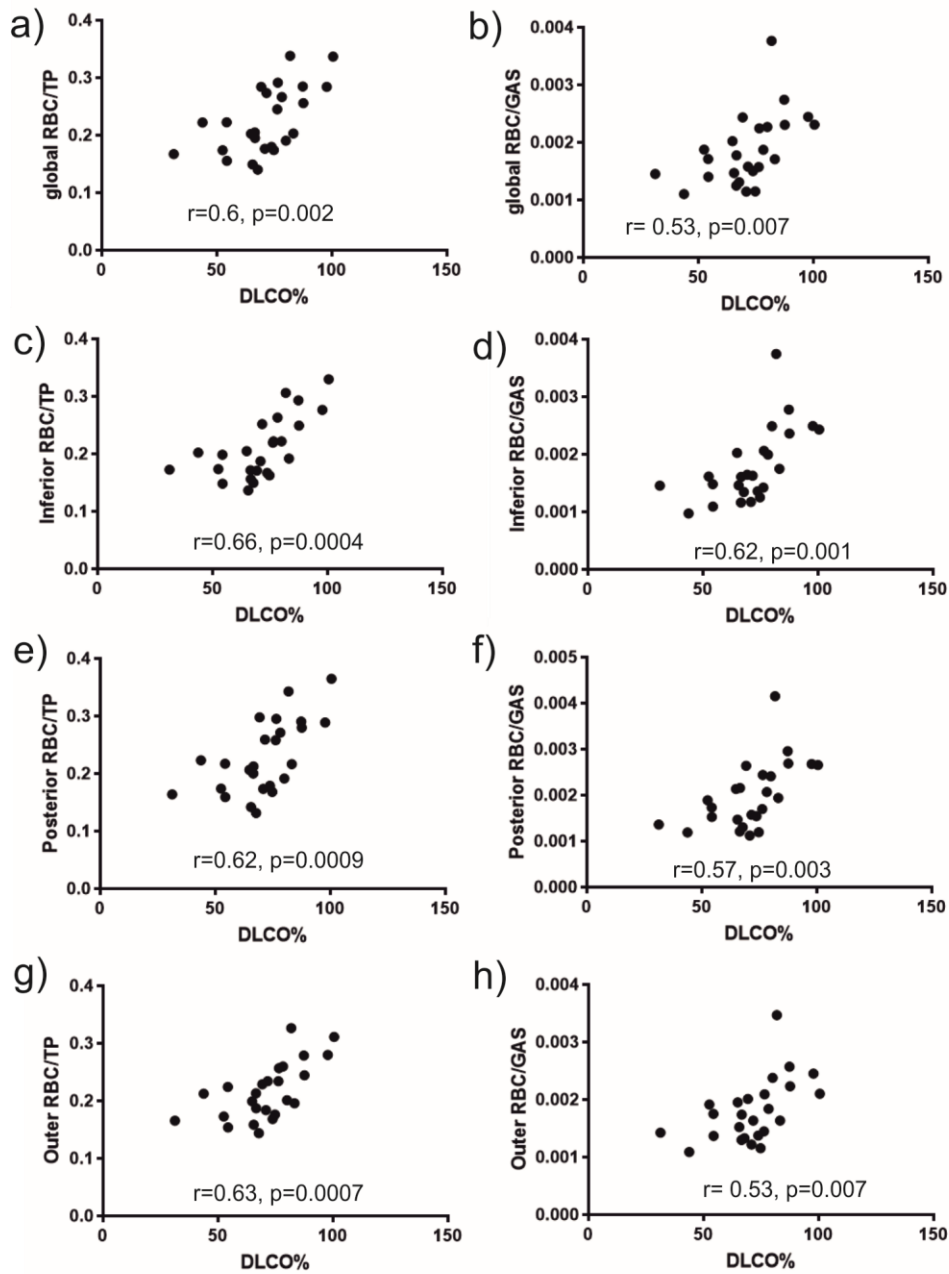
Figure 7: Pearson correlation of global RBC/TP ratio (a) and RBC/GAS ratio (b) with the diffusing capacity of the lung for carbon monoxide DL_{CO}%. c) to h): same correlation plots when using the average ratios of the inferior, posterior and outer parts of the lung.